Two-Dimensional Gapping to Reduce Light-Load Loss of Point-of-Load Inductor

Ting Ge, *Student Member, IEEE*, Khai D. T. Ngo, *Fellow, IEEE*, and Jim Moss, *Member, IEEE*

***Abstract*—Point-of-load converter at light load has low efficiency owing to the "fixed losses" such as core loss and ac winding loss. This paper focuses on two-dimensional (2-D) gapping of a ferrite core to shape inductance versus load current to reduce inductor loss at light load. Since the maximum inductance of conventional stepped gap is limited by the cross-sectional area of the thin gap, a 2-D gap is formed by joining two orthogonal gaps to gain flexibility. Higher inductance is achieved at light load compared with uniform-gap and stepped-gap geometries having the same volume and dc resistance. AC resistance is reduced at light load thanks to a magnetic path that steers ac flux away from the winding. Two *C*-cores with 2-D gap were fabricated and tested on a buck converter with 50% reduced total inductor loss at 10% load current.**

***Index Terms*—2-D gap, nonlinear inductance, loss at light load, swinging inductor.**

NOMENCLATURE

B_C	Magnetic flux density for *C*-cores at nominal load.
B_I	Magnetic flux density for *I*-bar in Fig. 3(c).
$B_{\mathrm{sat}C}$	Saturated magnetic flux density for *C*-cores in Fig. 3(c).
C_m, x, and y	Core loss coefficients.
c and k_B	Fitting parameters for $\mu_{Ir} - B_I$ curve.
D	Duty cycle.
H_{dc}	DC component of magnetic field intensity.
h	Core thickness.
I_{dc}	DC current of the inductor.
I_{initial}	Initial current in simulation.
I_{knee}	Knee current.
I_{load}	Load current.
I_{rms}	RMS value of inductor current.
I_{Lp-p}	Peak-to-peak current through the inductor.
K_{dc}	DC effect on core loss density.
$L_{\max}$	Inductance at zero current.
$L_{\min}$	Inductance at nominal load.
l_{A1}	Width of thin gap in stepped gap or width of *I*-bar in 2-D gap.
l_{A2}	Half width of middle leg in 2-D gap.
l_{A3}	Half of core height minus l_{g1} for 2-D gap.
l_{A4}	Width of the side leg.
l_c	Effective length in the *C*-cores.
l_g	Length for uniform gap.
l_{g1}	Thin gap's length in stepped gap.
l_{g2}	Thick gap's length in stepped gap and 2-D gap.
l_{g3}	Thin gap's length in 2-D gap.
N	Number of turns.
$P_{w\mathrm{ac}}$	AC winding loss.
P_{wt}	Total winding loss.
P_{v0}	Core loss density without biased effect.
P_v	Core loss density with biased effect.
R_{ac}	AC resistance.
R_c, R_I, R_{g1}, R_{g2}, and R_{g3}	Reluctances for *C*-cores, *I*-bar, and gaps (l_{g1}, l_{g2}, and l_{g3}).
R_{dc}	DC resistance.
V_{Lp-p}	Peak-to-peak voltage across the tested inductor.
α	Ratio between the inductance at I_{knee} and $L_{\max}$.
μ_0	Permeability for air.
μ_r	Relative permeability.
μ_{Ir}	Relative permeability of *I*-bar.
φ_1, φ_2	Magnetic flux.

I. INTRODUCTION

THE efficiency of a power converter usually drops at light load [1]–[3]. Among the reasons for the degradation are the inductor's losses that do not scale down with load current [4]. Without considering the dc bias, the core loss [5] is determined by the inductor's voltage and remains relatively constant as load current varies. Ferrite is employed herein to keep core loss low. The material chosen is P-ferrite which has low core loss density at 500 kHz. A ferrite core would need a (air) gap to control inductance, but this gap could adversely affect the other fixed loss which is the loss $P_{w\mathrm{ac}}$ associated with ripple current [6]–[8]. Since $P_{w\mathrm{ac}}$ is related to ac resistance R_{ac} and ripple current I_{ac} by $P_{w\mathrm{ac}} = R_{\mathrm{ac}} I_{\mathrm{ac}}^2$, it can be decreased by reducing R_{ac} or I_{ac}. This paper will address how to shape and design the gaps to control full-load inductance, to swing the inductance up at

---

Manuscript received November 16, 2015; revised January 24, 2016; accepted February 17, 2016. Date of publication March 2, 2016; date of current version September 16, 2016. This work was supported by Texas Instruments. Recommended for publication by Associate Editor J. Acero.

T. Ge and K. D. T. Ngo are with the Center for Power Electronics Systems, Bradley Department of Electrical and Computer Engineering, Virginia Tech, Blacksburg, VA 24061 USA (e-mail: gting@vt.edu; kdtn@vt.edu).

J. Moss is with Texas Instruments, Santa Clara, CA 95051 USA (e-mail: Jim.Moss@ti.com).

Color versions of one or more of the figures in this paper are available online at http://ieeexplore.ieee.org.

Digital Object Identifier 10.1109/TPEL.2016.2537273

light load to reduce $I_{\rm ac}$, and to steer fringing flux from the gaps away from the winding at light load to reduce $R_{\rm ac}$. Core loss is analyzed to quantify its significance at light load as ac winding loss decreases.

Several methods have been reported to vary inductance with current. A simple way is to use two windings, one sustaining the main current and the other controlling the saturation level [9]–[12]. The extra winding adds loss and volume. Composite material that contains ferrite and powder iron can have current-dependent inductance. Commercial composite inductor in [13] shows high swinging, but the volume almost doubles that of constant inductors with the same current rating and dc resistance. Replacement of the air gap by magnetorheological (MR) fluid can also provide swinging inductance [14], [15]. Another solution is the use of low-temperature cofired ceramic (LTCC) with permeability dropping gradually [6]. All these methods have high core loss that originates from powder iron, MR fluid, or LTCC. Several gapping methods, like stepped gap or sloped gap, are available for ferrite core to realize step-shaped inductance with low core loss [16]–[19]. Their maximum inductance is limited by the thin gap.

In this study, a uniform-gap ferrite inductor is retrofitted with a 2-D gap to realize high swinging and low loss at light load without modifying the volume or the dc resistance. A thin gap is placed orthogonally to the existent thick gap to take advantage of the significantly larger cross-sectional area in the orthogonal direction. The thick gap is assumed horizontal and the thin gap vertical in the remainder of this paper. Inductance, core loss, and winding loss are optimized simultaneously to minimize the total loss at light load. The tradeoff between inductance swinging and saturation is analyzed to optimize the thickness of saturable piece. Finite-element simulation is the primary tool to deal with ac winding loss, bias-dependent and frequency-dependent core loss, and nonlinearity owing to saturation.

In Section II, the material and application circuit are reviewed; the 2-D gap inductor is delineated and compared with inductors using 1-D gaps (thick gap, thin gap, and stepped gap); simulated inductances and losses versus current are analyzed for all four cases. A design procedure for the inductor with 2-D gap is depicted in Section III along with a design example. Experimental results are discussed in Section IV to verify theory and simulation.

II. 2-D GAPPING TO ACHIEVE HIGH SWINGING AND LOW LOSSES

Inductors with 2-D gap and 1-D gaps (thick gap, thin gap, and stepped gap) are described and compared using the same application circuit, magnetic material, outer core dimensions, dc resistance, rated current, and voltage excitation. These gapping methods are evaluated using the buck converter shown in Fig. 1. The switching frequency is 500 kHz; the input voltage, 10 V; the output voltage, 5 V; and the nominal load current, 5 A. The two MOSFETs are BSC080N03LS with $R_{ds(\rm on)} = 8$ mΩ and voltage rating of 30 V from Texas Instruments. They are driven synchronously and in continuous-conduction mode. The inductance at rated current is $L = 4.7$ μH. The capacitors are $C_{\rm in} = 10$ μF and $C_{\rm out} = 10$ μF. With these parameters, the current ripple through the inductor is 1 A, and the voltage ripple across the output is 25 mV. Conventional and 2-D gap geometries are described next so that their impacts on inductor's loss at light load can be compared in Section II-B.

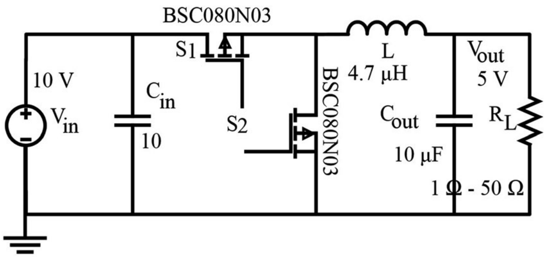

Fig. 1. Buck converter (switched at 500 kHz and outputting 25 W) used to compare gapping methods.

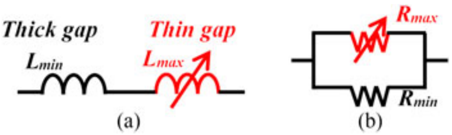

Fig. 2. Swinging inductor modeled by (a) serial inductances and (b) parallel reluctances.

A. Gap Geometries and Inductance Swing

The nonlinear mechanism of a swinging inductor with multiple gaps is explained by the constant reluctance that represents a single thick gap in series with a variable reluctance that represents a single thin gap shown in Fig. 2. A sufficiently thick gap would be able to contain most of the energy and keep the inductance relatively constant over the load range. A thin gap can store only a part of the required energy; the balance of the energy is stored in the ferrite core [20], [21]. The inductance is then controlled by the nonlinear permeability (and the gap length), giving rise to the swinging behavior. To realize high-current rating from the thick gap and inductance swinging from the thin gap, the two gaps are employed in one core to behave as a swinging inductor modeled by the series inductances in Fig. 2(a) and the dual parallel reluctances in Fig. 2(b). Light-load inductance $L_{\max}$ is determined by the thin gap while the core is not saturated, and inductance at nominal load $L_{\min}$ is determined by the thick gap after the thin gap is saturated. Larger dimensions (cross-sectional area and length) of the gap are beneficial for current-handling capability and swinging factor, but the increased volume is undesirable. Alternatives for gap placement to achieve wide inductance range without compromising energy density are studied.

The thick and thin gaps that are in line are termed "1-D gap" or "stepped gap" as shown in Fig. 3(b). The gap shown in Fig. 3(a) is a special case of 1-D gap where either the thin gap or the thick gap is eliminated. The equivalent circuit for Fig. 3(b) is a constant inductor in series with a swinging inductor as shown in Fig. 2(a). If the width $2l_{A4}$ of the middle leg for the

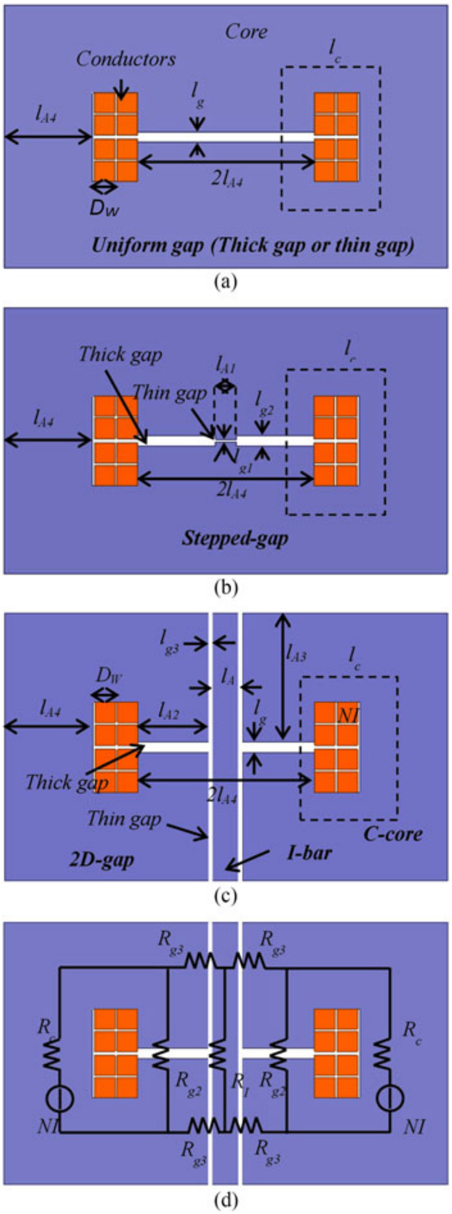

Fig. 3. 2-D plot of (a) constant gap design, (b) stepped-gap design, and (c) 2-D gap design with (d) equivalent reluctance network. They all have the same outer dimensions (10.8 mm × 6.5 mm × 3.5 mm) and dc resistance (11.8 mΩ).

E core in Fig. 3(b) is fixed, an increase in the width l_{A1} of the thin gap to improve light-load inductance $L_{\max}$ causes a corresponding decrease in the width of the thick gap, resulting in loss of nominal-load inductance $L_{\min}$. Another disadvantage of the stepped gap is that the magnetic area around the thin gap would be saturated at heavy load. As the l_{A1} increases, the whole core would be saturated gradually. Even if the specified nominal-load inductance could be satisfied, e.g., a uniform thin gap with $l_{A1} = 2l_{A4}$, saturation would bring high bias-dependent core loss, which will be discussed in Section II-B.

In order to overcome the restriction on maximum inductance for stepped gap, and to gain more freedom in controlling the gap dimensions, the inductor with "2-D gap" illustrated in Fig. 3(c) places the thin gap perpendicular to, instead of in-line with, the thick gap to take advantage of a larger cross-sectional area ($l_{A3} > l_{A1}$) to achieve higher inductance at light load with the same thin-gap's length. One *I*-bar in Fig. 3(c) is inserted between two *C*-cores to construct the vertical thin gaps, behaving as a swinging reluctance R_{g3} in Fig. 3(d). The choice of stepped gap or 2-D gap depends on the aspect ratio of the core. The 2-D gap is advantageous when the core's aspect ratio is close to unity since the volume in two dimensions stores more energy and yields higher swinging than one dimension. As mentioned earlier, the l_{A1} in the stepped gap determines the tradeoff between the light-load inductance and saturation level at nominal load. The 2-D gap decouples the two effects by using two independent and orthogonal geometrical parameters, the thickness of the *I*-bar and the cross-sectional area for the thin gap. The light-load inductance then relies only on l_{A3} and l_{g3}; and the bias level at nominal load can be designed by l_{A1}.

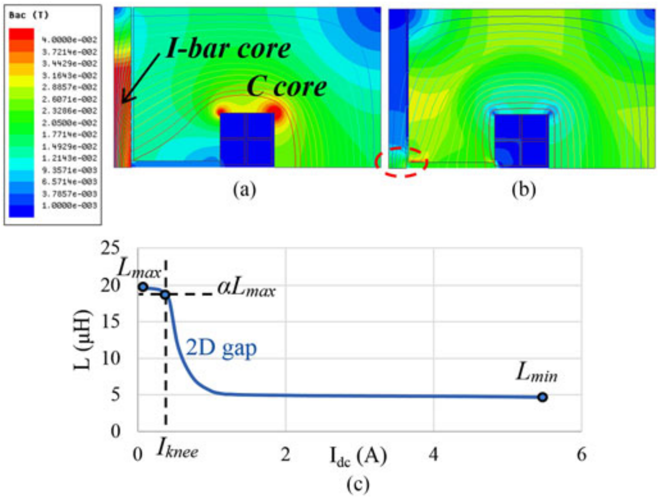

Fig. 4. Simulated ac flux density at (a) $I_{\rm dc} = 0.1$ A and (b) $I_{\rm dc} = 5$ A for one-fourth model of 2-D gap shown in Fig. 3(c) with $l_{g3} = 0.05$ mm, $l_{g2} = 0.25$ mm, $l_{A4} = 2.15$ mm, and $l_{A1} = 0.7$ mm; (c) simulated inductance versus dc current. Core material is P-ferrite described in Section II-B.

Inductors employing thin gap, stepped gap, and 2-D gap exhibit swinging behavior via similar mechanisms. This is explained by the distributions of ac magnetic flux density $B_{\rm ac}$ at light load and nominal load for the 2-D gap in Fig. 4(a). The materials used in the simulation are described in Section II-B. At light load where no core saturates, the *I*-bar is a part of a low-reluctance path [$R_{g3} - R_c - R_I$ in Fig. 3(d)] that not only yields high inductance, but also steers ac flux away from the conductors to lower ac resistance. The higher flux density in the *I*-bar incurs more core loss, but core loss will be shown negligible to winding-loss reduction in the next section. At nominal current, the *I*-bar in Fig. 3(c) would be saturated, and has low permeability as well as low ac flux density as shown in Fig. 4(b). The reluctance path then transfers to "$R_{g2} - R_c - R_{I}$." The fringing flux in the winding window induces higher ac resistance, but core loss is reduced thanks to lower $B_{\rm ac}$ in the *I*-bar. Small ac flux caused by the fringing flux remains in the *I*-bar at the region close to the intersection of the two orthogonal gaps. The

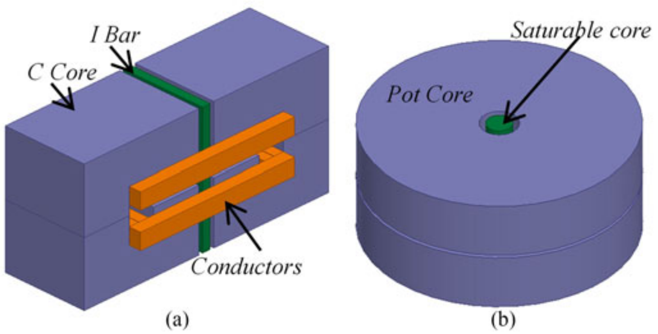

Fig. 5. Two 3-D candidates of 2-D gap design: (a) Two *C*-cores with saturable bar and (b) pot core with saturable cylinder.

equivalent cross-sectional area for the thick gap is increased, and the nominal-load inductance is comparable to that of the inductor with uniform, thick gap. This is the key reason for the inductor with 2-D gap achieving swinging inductance without losing heavy-load inductance within the same volume. Since the *I*-bar absorbs significant fringing flux at nominal load, ac winding resistance is lower than that in 1-D-gapped inductor.

The parameters $L_{\max}, L_{\min}$, and I_{knee} defined in Fig. 4(c) characterize the inductance swinging of the 2-D gap. The light-load inductance $L_{\max}$ is defined as the inductance at zero current, derived by R_{g3}, R_I, R_{g2}, and R_c in Fig. 3(d). The reluctances R_I and R_c are negligible at light load since both *C*-cores and *I*-bar have high permeability. The dimensions of the gaps are selected such that $lg_3/l_{A3} << lg_2/l_{A3}$ to make $R_{g3} << R_{g2}$. Fringing effect is neglected since the thin gap's length is much smaller than the height of *I*-bar in Fig. 3(c). Then, $L_{\max}$ is approximated by

$$L_{\max} = \frac{N^2}{(R_{g3}+R_I)//\left(\frac{1}{2}R_{g2}\right)//\left(\frac{1}{2}R_c\right)} \approx \frac{N^2}{R_{g3}}$$
$$= \frac{N^2 l_{A3} h \mu_0}{l_{g3}} \left(\frac{l_{g3}}{l_{A3}} \ll \frac{l_{g2}}{l_{A2}}\right) \tag{1}$$

where *N* is the number of turns; μ_0 is the air permeability; and *h* is the core thickness.

The nominal-load inductance $L_{\min}$ depends on R_{g2} and R_c. Since $R_c << R_{g2}$, the minimum inductance is approximately

$$L_{\min} = \frac{N^2}{\left(\frac{1}{2}R_{g2}\right)//\left(\frac{1}{2}R_c\right)} \approx \frac{N^2(2l_{A2}+l_{g2})(h+l_{g2})\mu_0}{l_{g2}} \tag{2}$$

where fringing effect is taken into account by extending the cross-sectional dimensions for the thick gap by l_{g2} [22].

Since the inductance at I_{knee} is still high, most of the flux goes through the *I*-bar and thin gap instead of the thick gap. Let B_I be the average magnetic flux density in the *I*-bar when the current is I_{knee}. The flux flowing through the cross-sectional areas $l_{A1}h$ and $l_{A3}h$ are $B_I l_{A1} h$. The current I_{knee} is given by

$$I_{\text{knee}} = \frac{l_{g3} B_I l_{A1}}{\mu_0 l_{A3} N}. \tag{3}$$

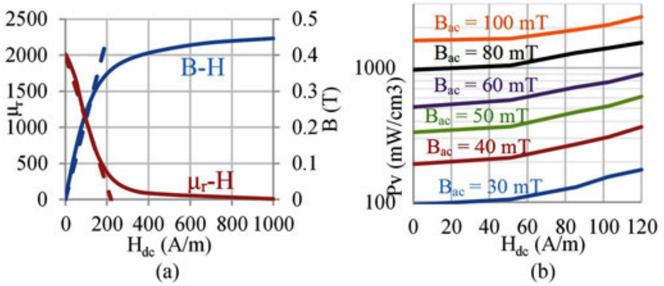

Fig. 6. (a) Relative permeability and (b) measured core loss density of P-ferrite versus H_{dc} at 500 kHz and 25 °C.

Two candidates to implement the 2-D gap are shown in Fig. 5. One is to insert a ferrite plate (*I*-bar) into the middle region for gapped *C*-cores. Between the *I*-bar and *C*-cores is the thin part of the 2-D gap. The thick part of the 2-D gap is orthogonal to the thin part and is embedded within the *C*-cores. The other structure is a pot core combined with one ferrite cylinder in the center hole. The thick gap is placed between the two core halves, whereas the thin gap surrounds the cylinder core. Note that (1)–(3) were derived for Cartesian coordinates; cylindrical coordinates need to be considered for pot cores. A drawback of the pot core with 2-D gap is the difficulty in controlling the thin gap's length.

B. Performance Comparison

The material for general gapped inductor is ferrite. Here, the material chosen is P-ferrite which has low core loss density at 500 kHz. Measured permeability, flux density, and core loss density are shown in Fig. 6. The saturated magnetic flux density is 0.45 T. Core loss is sensitive to dc bias, especially when the core is saturated [24]–[33]. The core loss versus dc bias in Fig. 6(b) was measured by two U cores (OP41106, P-ferrite) with one winding for the dc excitation (0–0.7 A), one winding for ac excitation with sinusoidal waveform, and the other winding for flux sensing. Each winding had five turns of 180 strands with a total diameter of 0.72 mm. Measurement procedure followed [34]. A capacitor in series with the tested inductor was used to cancel the passive component of the voltage to improve phase accuracy. This capacitor was adjusted with dc current based on the measured permeability curve in Fig. 6(a).

The dependence of core loss density P_v on dc magnetic field intensity H_{dc} is accounted for by the function $K_{\mathrm{dc}}(H_{\mathrm{dc}})$ [35]

$$P_v = P_{v0} K_{\mathrm{dc}}(H_{\mathrm{dc}}) \tag{4}$$

where P_{v0} is the core loss without dc effect, which can be calculated by such models as MSE [36], GSE [37], iGSE [38], or RESE [39]. Here, the model [40] native to the finite-element simulator is used since it deals with the dynamic core loss for 2-D or 3-D conveniently via the core loss parameters C_m, *x*, and *y* extracted from the loss curve associated with sinusoidal excitation. It takes into account minor loops to predict instantaneous hysteresis loss. The model parameters can be extracted from standard loss curves, e.g., $C_m = 6.22 \times 10^{-3}$, $x = 1.93$, and $y = 2.66$ for P-ferrite.

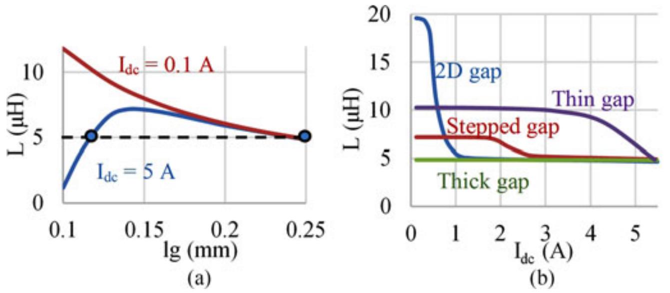

Fig. 7. (a) Simulated L versus gap length for uniform gap and (b) simulated L versus I_{dc} for 2-D gap with the dimensions in Fig. 4, stepped gap ($l_{g1} = 0.05$ mm and $l_{g2} = 0.25$ mm), thin gap ($l_g = 0.116$ mm), and thick gap ($l_g = 0.25$ mm) with structures in Fig. 3.

Core loss density was measured as a function of H_{dc} and plotted in Fig. 6(b). The magnitude of the magnetic flux density in the design example is close to 30 mT. Curve fitting yields

$$\begin{aligned} K_{\mathrm{dc}}\left(H_{\mathrm{dc}}\right) &= 0.000075H_{\mathrm{dc}}^2 - 0.00203H_{\mathrm{dc}} + 1, \\ \text{for } B_{\mathrm{ac}} &= 30\ \mathrm{mT} \end{aligned} \tag{5}$$

where H_{dc} is the dc component of magnetic field intensity in A/m.

The specifications of input voltage equal to 10 V and output voltage equal to 5 V determine the duty cycle *D*. The core loss density for rectangular voltage versus duty cycle with a fixed flux density [39] is calculated by

$$P_{v\_\mathrm{rect\_fixed}B} = \frac{8}{\pi^2 \left[4D\left(1-D\right)\right]^{\gamma+1}} C_m f^x B_{\mathrm{ac}}^y \tag{6}$$

where $\gamma = 0$ for sinusoidal excitation, and $0 < |\gamma| < 1$ [39] for triangular flux density. The core loss density is minimum at $D = 0.5$ for fixed B_{ac}. If flux density varies with *D* to adjust the output voltage for a fixed input voltage, the core loss density is

$$\begin{aligned} P_{v\_\mathrm{rect\_}V\mathrm{in}} &= \frac{8}{\pi^2 \left[4D\left(1-D\right)\right]^{\gamma+1}} C_m f^x \left[\frac{V_{\mathrm{in}}\left(1-D\right)D}{2f}\right]^y \\ &= \frac{8^{1-y}}{\pi^2 \left[4D\left(1-D\right)\right]^{\gamma+1-y}} C_m f^{x-y} V_{\mathrm{in}}^y. \end{aligned} \tag{7}$$

Since $|\gamma| < 1$ and $y > 2$, maximum core loss density occurs at $D = 0.5$ for fixed V_{in}; this will be confirmed later in this section.

The nonlinear permeability of the core material gives possibility to realize swinging inductance by using only one gap [20]. Two gaps to implement the required inductance at heavy load (e.g., $L = 5\ \mu$H at 5 A) are shown in Fig. 7(a). The inductance for the thick gap at $l_g = 0.25$ mm is constant, whereas the thin gap at $l_g = 0.114$ mm yields swinging inductance. Simulated inductances for four cases (2-D gap, stepped gap, thin gap, and thick gap) are shown in Fig. 7(b). The 2-D gap and stepped gap have the same thin gap's length and thick gap's length. The 2-D gap has the swinging factor up to four although the knee current is relatively small, which is suitable for point-of-load converter working at two load conditions to improve efficiency as reported in [16]. The inductance for the thin gap is higher than that of stepped gap thanks to its larger effective cross-sectional area at light load. However, the saturation of the thin gap at nominal load would decrease the inductance quickly, and bring higher core loss.

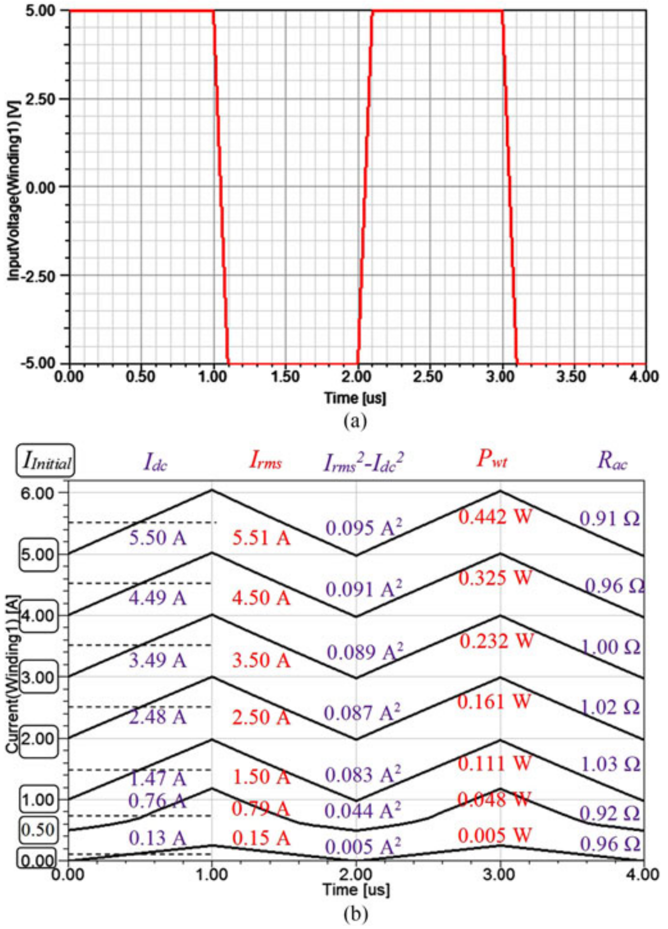

Fig. 8. (a) Voltage excitation and (b) simulated current waveforms labeled by $I_{\mathrm{initial}}, I_{\mathrm{dc}}, I_{\mathrm{rms}}, I_{\mathrm{rms}}^2 - I_{\mathrm{dc}}^2, P_{\mathrm{wt}}$, and R_{ac} for 2-D gap with the structure in Fig. 3 and gapping parameters in Fig. 4.

DC winding loss is dominant at nominal load since ripple current is negligible compared with dc current. The four cases have almost the same winding loss at nominal load as shown in Fig. 9(b) by specifying the same dc resistance. As dc current decreases, the winding loss is dominated by the ac ripple and ac resistance. The 2-D gap with the highest inductance at light load shown in Fig. 7(b) has the lowest ac ripple. The ac resistance R_{ac} is calculated from

$$P_{\mathrm{wt}} = I_{\mathrm{dc}}^2 R_{\mathrm{dc}} + \left(I_{\mathrm{rms}}^2 - I_{\mathrm{dc}}^2\right) R_{\mathrm{ac}}. \tag{8}$$

Transient finite-element simulation was employed to extract R_{ac} versus I_{dc} as visualized in Fig. 8. The inputs were the voltage waveform in Fig. 8(a) and the initial current I_{initial} which were swept from 0 to 5 A [see Fig. 8(b)]. The corresponding current waveforms, dc currents I_{dc}, rms currents I_{rms}, and total winding loss P_{wt} (including all harmonics) are tabulated in Fig. 8(b). With R_{dc} derived from finite-element simulation, R_{ac} (including all harmonics) is calculated from (8) and tabulated in Fig. 8(b). The average R_{ac} is 0.97 Ω with

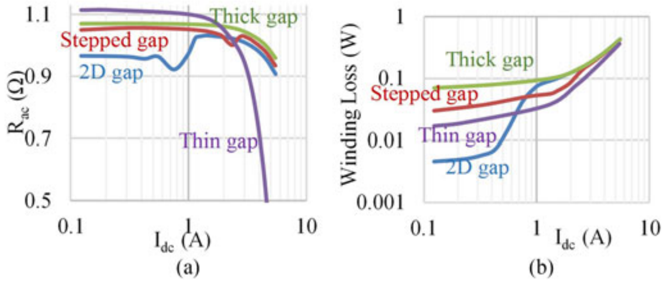

Fig. 9. (a) Simulated ac resistance R_{ac} and (b) total winding loss versus dc current for 2-D gap, stepped gap, thin gap, and thick gap with structures in Fig. 3 and gapping parameters from Fig. 4.

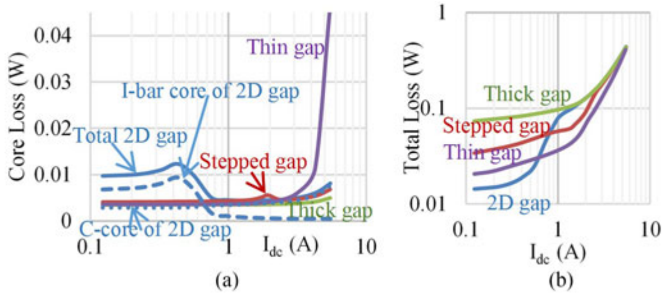

Fig. 10. (a) Simulated core loss and (b) total inductor loss versus dc current for 2-D gap, stepped gap, thin gap, and thick gap with structures in Fig. 3 and gapping parameters from Fig. 4.

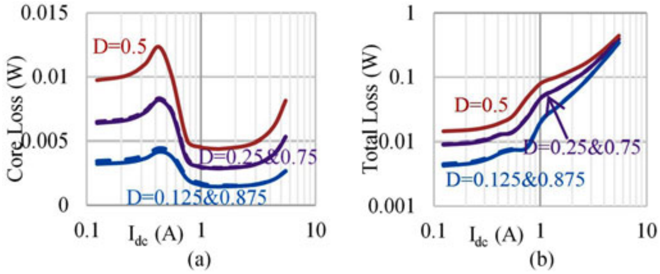

Fig. 11. Simulated (a) core loss and (b) total loss versus dc current and duty cycle D for 2-D gap in Fig. 3 and gapping parameters from Fig. 4.

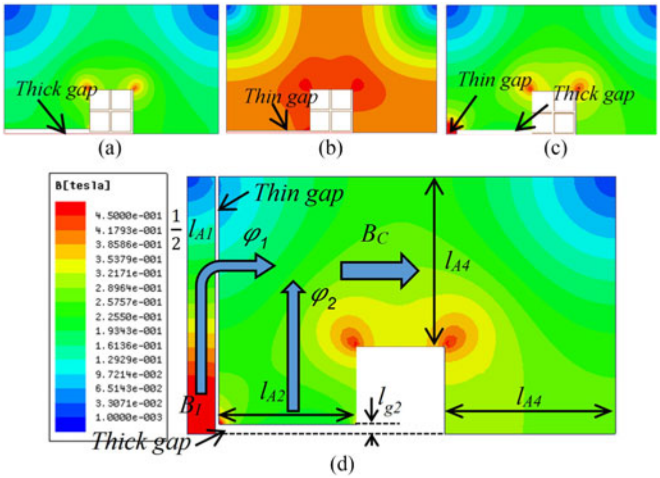

Fig. 12. Simulated dc flux density of (a) thick gap, (b) thin gap, (c) stepped gap, and (d) 2-D gap at $I_{\mathrm{dc}} = 5$ A for one-fourth model with structures in Fig. 3 and gapping parameters in Fig. 4.

6% variation for triangular current. The inductor was also simulated with sinusoidal voltage. The observed average R_{ac} (with sinusoidal excitation) was 0.86 Ω with 7% variation.

The ac resistance of 2-D gap is small at light load because the flux lines are steered into the *I*-bar and away from the windings as shown in Fig. 4(a). The ac resistance drops as the current increases as shown in Fig. 9(a) thanks to an increase in equivalent gap length and a decrease in field strength [41].

The ac flux lines transfer to the thick gap after the *I*-bar saturates as illustrated in Fig. 4(b), inducing fringing flux in the winding window and high ac resistance. The further increasing current at heavy load would increase bias level of *C*-cores, and reduce the field intensity in the winding window. The ac resistance drops again with similar mechanism as the first dip.

Core loss was simulated for four cases considering the frequency-dependent and bias-dependent nonlinearities. Voltage excitation was an ideal rectangular waveform based on the circuit from Fig. 1. The core loss density P_{v0} and average magnetic field intensity H_{dc} for each element were simulated by FEA. Core loss density with dc effect at each element was then calculated by using the P_{v0} and H_{dc} in the model from (4) and (5). Total core loss was derived by the volume integration of core loss density. For the stepped gap and thick gap, core loss is almost constant because the distribution of flux density does not change significantly. The high dc bias for thin gap at heavy load leads to saturation shown in Fig. 12(b) and high core loss in Fig. 10(a). The inductor with 2-D gap shows high core loss at light load resulted from the *I*-bar, which is demonstrated by separating the core loss from *I*-bar and that from the *C*-cores illustrated in Fig. 10(a). One effective way to reduce the light-load core loss is to utilize the material with low loss density. Another method described in Section II-C is to adjust the thickness of the *I*-bar to move the peak core loss to higher current. Total loss plotted in Fig. 10(b) is dominated by winding loss at light load for all cases except the 2-D gap which has significant reduction of winding loss.

The core loss and total loss versus duty cycle and dc current for 2-D gap are plotted in Fig. 11. Highest core loss and total loss are incurred for $D = 0.5$ owing to high B_{ac}, confirming that $D = 0.5$ is the worst case for buck converter [39].

The dc flux density was also simulated to evaluate the operation at nominal load. Without the thin gap, the whole core has no significant hot points as shown in Fig. 12(a). The magnetic segments adjacent to the thin gaps in Fig. 12(c) and (d) saturate first, and saturation could spread into the magnetic regions in series with the thick gaps unless the core is properly designed (see Section II-C). Once the *I*-bar in the 2-D-gapped inductor saturates, the ac flux prefers to flow through the *C*-cores and the thick gap. The *I*-bar then carries negligible ac flux and enjoys low core loss although it is biased by high dc magnetic field intensity. A design priority is to keep the *C*-cores away from saturation to avoid high bias-induced core loss. This will be described in Section II-C. The dc flux density for the uniformly

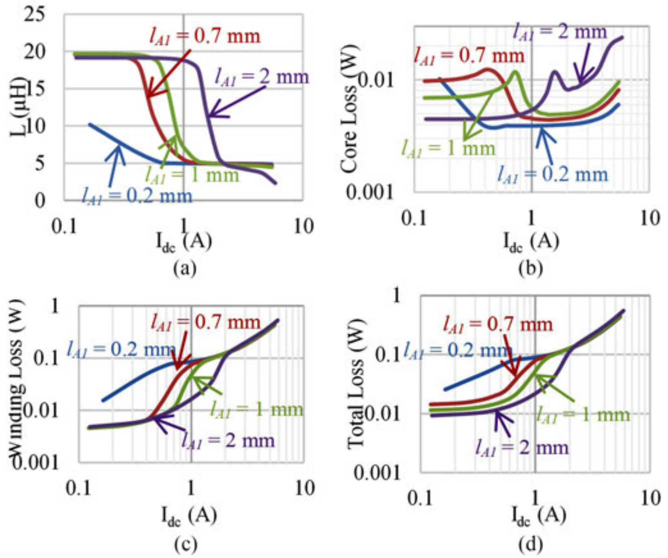

Fig. 13. Simulated (a) inductance, (b) core loss, (c) winding loss, and (d) total loss versus dc current for 2-D gap with geometry in Figs. 3 and 4, parametric with thickness of *I*-bar (l_{A1}).

thin gap is relatively high as illustrated in Fig. 12(b). If the core were saturated, core loss and temperature would increase, leading to thermal run away.

C. Choice of Thickness for I-Bar

The impact of the *I*-bar's thickness on inductance and loss was assessed numerically to establish design criteria for l_{A1}. Inductance, core loss, winding loss, and total loss are plotted versus load current and l_{A1} in Fig. 13. More current is needed to saturate a thicker *I*-bar. An advantage of this is an increase in $I_{\rm knee}$ [see Fig. 13(a)], i.e., the range of light load that enjoys lower winding loss is broadened [see Fig. 13(c)]. Core loss also decreases with l_{A1} as illustrated in Fig. 13(b). An increase in the cross-sectional area of the *I*-bar, however, means more flux would enter the *C*-cores [see Fig. 12(d)] and the risk of saturation would increase at nominal load current. This is evident for the curve corresponding in Fig. 13(a), which is lower than the specified nominal-load inductance. Winding loss and bias-dependent core loss would increase with l_{A1} at nominal load as shown in Fig. 13(c) and (b), respectively. In order to avoid the saturation issue, the dc flux density in the *C*-cores should be estimated at the beginning of design, followed by the equations to calculate l_{A1} as discussed in the latter part of this section.

The dc flux density B_C in the *C*-cores under nominal load is derived from the dc flux φ_1 through the *I*-bar, φ_2 through the thick gap, and $l_{A4}hB_c$ through the *C*-cores as illustrated in Fig. 12(d). The contribution of the saturated *I*-bar to nominal-load inductance is negligible, i.e., $L_{\min}$ is dominated by the thick gap. The dc flux φ_1 is assumed to retain the value $L_{\max}I_{\rm knee}/2N$ attained at $I_{\rm knee}$, whereas φ_2 is approximated by $L_{\min}I_{\rm load}/2N$. The approximate expression for B_C is then

$$B_C = \frac{\varphi_1+\varphi_2}{l_{A4}h} \approx \frac{1}{2Nhl_{A4}}\left(L_{\max}I_{\rm knee} + L_{\min}I_{\rm load}\right). \quad (9)$$

The last equality in (9) constrains the specifications of $I_{\rm knee}, L_{\max}$, and $L_{\min}$, especially since B_C should be lower than saturation flux density to limit core loss. Since $I_{\rm knee}$ is proportional to l_{A1} via (3), larger l_{A1} leads to larger B_C and higher bias-dependent core loss.

The *B–H* curve and $\mu_r - H$ curve are approximately linear before saturation as seen in Fig. 6(a), i.e., μ_{rI} is linearly related to B_I

$$\mu_{rI} = c - k_B B_I \quad (10)$$

where μ_{Ir} is the relative permeability in the *I*-bar; $c = 2000$ and $k_B = 3700$ [1/T] for the P-ferrite in Fig. 6(a). The current $I_{\rm knee}$ and the corresponding inductance $\alpha L_{\max}, 0 < \alpha < 1$, characterize the inductance droop caused by saturation of the *I*-bar. Since the inductance at $I_{\rm knee}$ is still high, most of the flux goes through the *I*-bar and thin gap instead of the thick gap. Since R_I is no longer negligible compared to R_{g3} at $I_{\rm knee}$

$$\alpha L_{\max} \approx \frac{N^2}{R_{g3}+R_I}. \quad (11)$$

From (1) and (11)

$$R_I = \frac{1-\alpha}{\alpha}R_{g3} \text{ at } I_{\rm knee}. \quad (12)$$

If the flux lines inside the *I*-bar [see Fig. 4(a)] are approximated to be elliptical [23]

$$R_I = \frac{4l_{A3} + (\pi-2)\,l_{A1}}{\mu_{Ir}\mu_0 h\left(\frac{l_{A1}}{2}+l_{A3}\right)\ln\left(\frac{l_{A1}}{2l_{g3}}\right)}. \quad (13)$$

Equations (1), (3), (10), and (13) are combined to yield a relationship from which l_{A1} is determined

$$\frac{1-\alpha}{\alpha} = \frac{4l_{A3}+(\pi-2)\,l_{A1}}{\left(cl_{g3} - k_B\frac{I_{\rm knee}\mu_0 l_{A3}N}{l_{A1}}\right)\left(\frac{l_{A1}}{2l_{A3}}+1\right)\ln\left(\frac{l_{A1}}{2l_{g3}}\right)}. \quad (14)$$

III. RETROFIT DESIGN PROCEDURE

An inductor with a uniform thick gap is assumed already available. The retrofit procedure outlined in Fig. 14 adds an *I*-bar and a 2-D gap to swing the inductance up to $L_{\max}$ below $I_{\rm knee}$, keeping inductance $L_{\min}$ and dc resistance at nominal load the same. The exterior dimensions, number of turns, material properties, and interior parameters l_{A3} and l_{A4} are inherited from the available inductor. Unknown parameters are l_{A1}, l_{g3}, and l_{g2}. The first step is to check the biased condition of B_c. If B_C is lower than maximum flux density $B_{{\rm sat}C}$ of *C*-cores, the design proceeds. Otherwise, the specifications of $L_{\max}, L_{\min}, I_{\rm knee}$, and $I_{\rm load}$ should be revised to meet (9). The gap l_{g3} between the *I*-bar and the *C*-core is determined by utilizing the inductance at light load in (1). The thickness l_{A1} is obtained from specified current $I_{\rm knee}$ in (14). The thick gap's length is calculated using the nominal-load inductance $L_{\min}$ and the associated cross-sectional area of the flux path.

To exemplify the design procedure, consider the retrofit of an existing inductor with $l_{A4} = 2.15$ mm, $l_{A3} = 3.125$ mm, $N = 8$, $B_{{\rm sat}C} = 0.45$ T, $h = 3.5$ mm, $L_{\max} = 18\ \mu$H, $L_{\min} = 4.5\ \mu$H,

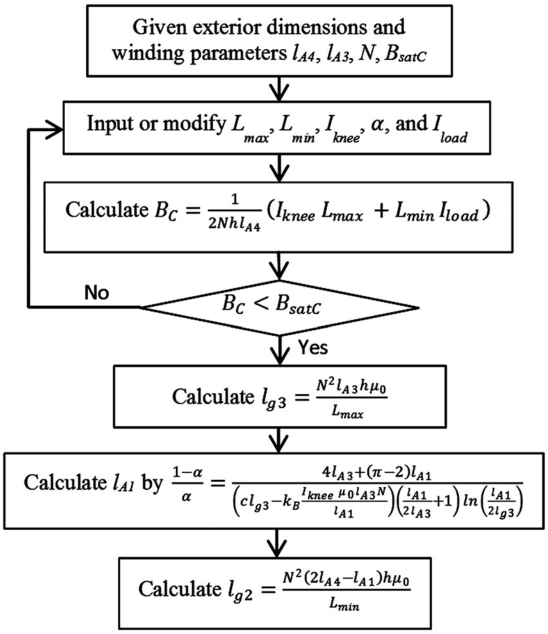

Fig. 14. Flowchart to design 2-D gap.

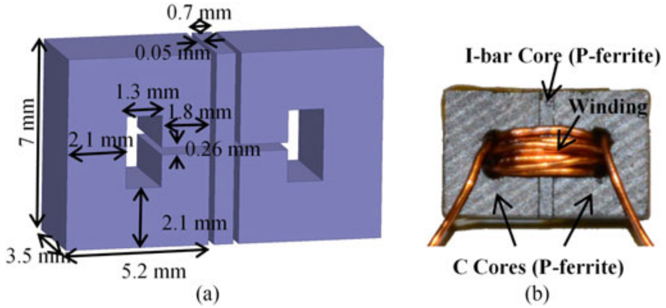

Fig. 15. (a) 3-D model and dimensions of (b) 2-D-gapped inductor in experiment with $N = 8$ and winding diameter of 0.46 mm.

$I_{\text{knee}} = 0.27$ A, $\alpha = 0.9$, and $I_{\text{load}} = 5$ A. Design results based on Fig. 14 are $B_C = 0.23\text{T} < B_{\text{sat}C}, l_{g3} = 0.049$ mm, $l_{A1} = 0.71$ mm and $l_{g2} = 0.23$ mm. The results agree with the example in Section II and the simulated results shown in Fig. 7(b).

IV. VERIFICATION

The inductor with 2-D gap was fabricated by two *C*-cores and one *I*-bar with the dimensions shown in Fig. 15(a) and customed hardware in Fig. 15(b). The material for these cores was P-ferrite from Magnetics, Inc. The number of turn was 8; the wire diameter, 0.46 mm (AWG 25); and dc resistance, 18 mΩ. The thin gap was realized by polyester film with thickness of 0.05 mm. The large wire diameter was chosen to reduce dc winding loss at full load. A smaller wire diameter (e.g., 0.33 mm) would incur twice the dc winding loss at full load and slightly higher total loss at light load, e.g., 26 versus 24 mW at $10\%I_{\text{load}}$.

The inductor prototype and a reference inductor without the *I*-bar were tested in a synchronous buck converter with the specifications in Fig. 1. To compare them fairly, the high-side MOSFET was hard switched within the load range. The current I_L through the inductor and voltage V_L across the inductor were measured to calculate inductor loss. When $I_{\text{dc}} << I_{\text{knee}}$ or $I_{\text{dc}} >> I_{\text{knee}}$, I_L is triangular as seen in Fig. 16(a) and (c) since the inductance is constant in those operating regions. When I_{dc} is close to I_{knee}, the current waveform contains harmonics as seen in Fig. 16(b) since inductance varies with instantaneous current in the range of the current ripple.

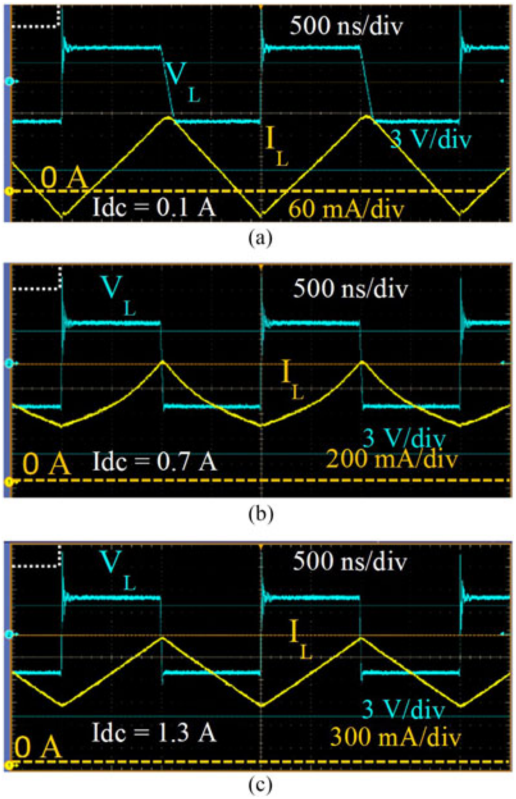

Fig. 16. Measured waveforms of the current through the inductor and the voltage across the inductor for the prototype in Fig. 15 tested in the buck converter in Fig. 1 at (a) $I_{\text{dc}} = 0.1$ A, (b) $I_{\text{dc}} = 0.7$ A, and (c) $I_{\text{dc}} = 1.2$ A.

The inductance is measured by

$$L = \frac{V_{Lp-p}\,(1-D)\,D}{I_{Lp-p}\,f_s} \tag{15}$$

where V_{Lp-p} is the peak-to-peak voltage across the tested inductor; I_{Lp-p} is the peak-to-peak current through the tested inductor; and D is the duty ratio. Error owing to dc resistance of the winding is avoided since L is calculated from the peak-to-peak V_L across the entire switching period.

The inductor power was measured by multiplying the instantaneous V_L by the instantaneous I_L. The waveforms were measured using the mixed-signal oscilloscope MSO5104B set in “HiRes” mode to increase vertical resolution above 11 bits. The current bias was calibrated by the Tektronix DMM4020 current meter with resolution of 0.1 mA. The dc voltage was calibrated by multiplying the dc resistance measured by the DMM4020 Ohmmeter by the dc current. The core loss could

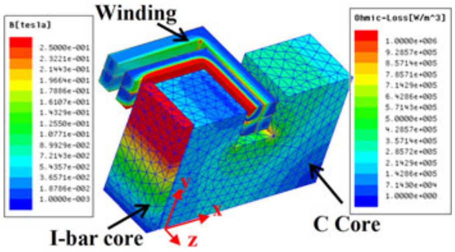

Fig. 17. 3-D-simulated ohmic loss and flux density at $I_{\mathrm{dc}} = 0.2$ A for one-eighth model of the inductor with 2-D gap in Fig. 15.

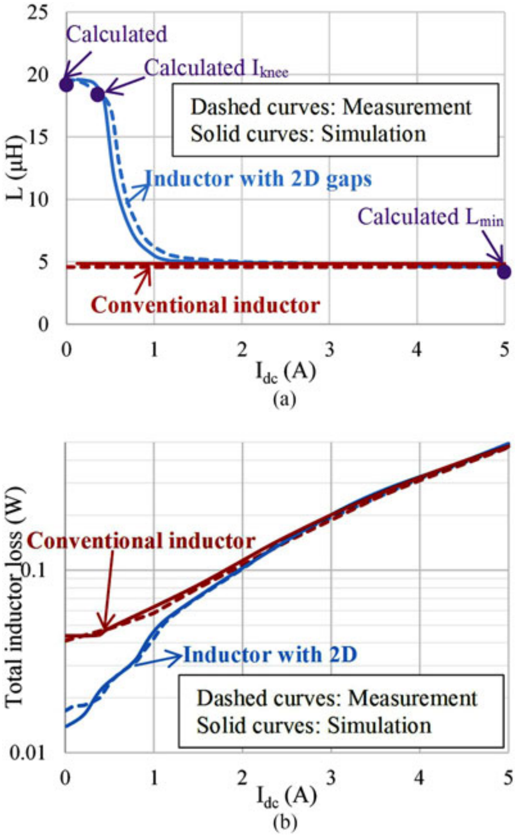

(a)

(b)

Fig. 18. Measured and simulated (a) inductances and (b) losses for a conventional inductor and an inductor with 2-D gaps; calculated $L_{\max}$, $L_{\min}$, and I_{knee} are also shown.

not be measured separately by the methods described in [42] since the tested inductor had only one winding.

While 2-D simulation is expeditious and reliable for nonlinear inductance and core loss, it cannot predict the variation of fringing field and the corresponding winding loss along the length of the conductor. 3-D finite-element simulation was thus employed to check the accuracy of 2-D simulation, and to characterize the experiment prototype. Fig. 17 shows a one-eighth model, taking advantage of the symmetrical boundary conditions. The loss density in the conductive regions near the *I*-bar is lower than that predicted by 2-D simulation thanks to reduced fringing field. The maximum mesh length for the core element is 0.5 mm, and the maximum mesh length for the conductor element is 0.1 mm. Each turn is individually closed by a square conductor to save computation time. The winding loss in 3-D simulation is roughly 20% less than that in 2-D simulation.

The measured and simulated inductances are compared in Fig. 18(a), and the measured inductor loss is compared with 3-D-simulated inductor loss in Fig. 18(b) for 0.46-mm wire diameter. The inductor with 2-D gap achieves three times the inductance and half the loss of the corresponding conventional inductor employing a 1-D thick gap for dc current lower than 0.5 A. If the wire diameter were thinner so that the wire could be placed away from the air gap to reduce fringing-induced loss, or if Litz wire were used, loss saving at light load is less pronounced. Simulation at $10\% I_{\mathrm{load}}$ with wire diameter of 0.33 mm reveals losses of 42 and 26 mW for 1-D and 2-D gaps, respectively, corresponding to 38% loss reduction. Two reasons can explain the loss error in the load range from 0 to 0.5 A for the case with 2-D gaps: the voltage ringing caused by the hard switching and phase error between voltage probe and current probe. The total loss at heavy load is dominated by the dc winding loss, which could be measured reliably and simulated with small error.

V. CONCLUSION

An inductor employing 2-D gap was constructed by two *C*-cores and one saturable piece, and tested in a point-of-load converter to demonstrate that the loss reduction could be as high as 50% at 10% rated current if the wire is thick to keep the loss low at heavy load. In order to achieve a high swinging inductance, a thin gap with small gap length and large cross-sectional area is needed. The gap length is limited by the fabrication tolerance, whereas the area depends on the location of the thin gap. If the thin gap is placed in-line (1-D) with the thick gap, as is the case for the "stepped gap," an attempt to increase light-load inductance would cause the core to saturate since an increase of the thin gap's area must be accompanied by a decrease of the thick gap's area. The 2-D gap arrangement essentially decouples the two effects by two independent and orthogonal geometrical parameters: the thickness of the *I*-bar and the cross-sectional area of the thin gap. The thickness can be designed to avoid saturation of the *C*-cores, whereas the large cross section available in another direction yields a higher light-load inductance.

The sacrifice of the core loss for the inductor with 2-D gap at light load is owing to the high ac flux in the *I*-bar. A peak core loss appears near the knee current where the permeability of the *I*-bar starts to drop. At nominal load, most of the core loss is incurred in the *C*-cores because of the redistribution of the ac flux density. The *I*-bar core would benefit from materials with low core loss density and less bias effect. The *C*-cores would benefit from materials with high saturation flux density for high power density. The core loss density for the *C*-cores is not critical since the winding loss and MOSFET loss are dominant in a point-of-load converter at nominal load.

Another approach to diminish the core loss is to shift the peak point to high current by increasing the thickness or flux density of *I*-bar based on (3). This, however, might induce saturation and bias-dependent core loss and thermal instability at nominal load via (9). The tradeoff between the light-load core loss and saturation level at nominal load should be monitored in the design of swinging inductor with 2-D gap to avoid additional loss at nominal load.

REFERENCES

[1] Y. Chen, P. Asadi, and P. Parto, "Comparative analysis of power stage losses for synchronous buck converter in diode emulation mode vs. continuous conduction mode at light load condition," in *Proc. IEEE Appl. Power Electron. Conf.*, Feb. 2010, pp. 1578–1583.

[2] A. Ball, M. Lim, D. Gilham, and F. C. Lee, "System design of a 3D integrated non-isolated Point of Load converter," in *Proc. IEEE Appl. Power Electron. Conf.*, Feb. 2008, pp. 181–186.

[3] Q. Li and F. C. Lee, "High inductance density low-profile inductor structure for integrated point-of-load converter," in *Proc. IEEE Power Electron. Spec. Conf. Rec.*, Feb. 2009, pp. 1011–1017.

[4] S. F. Lim and A. M. Khambadkone, "Non-linear inductor design for improving light load efficiency of boost PFC," in *Proc. IEEE Energy Convers. Congr. Expo.*, Sep. 2009, pp. 1339–1346.

[5] W. G. Hurley and W. H. Wölfle, *Transformers and Inductors for Power Electronics: Theory, Design and Applications*, 1st ed. Chichester, U.K.: Wiley, Feb. 2013, pp. 204–212.

[6] M. H. Lim, J. D. Van Wyk, F. C. Lee, and Z. Liang, "Internal geometry variation of LTCC inductors to improve light-load efficiency of DC-DC converters," *IEEE Trans. Compon. Packag. Technol.*, vol. 32, no. 1, pp. 3–11, Mar. 2009.

[7] L. Wang, Y. Pei, X. Yang, and Z. Wang, "Improving light and intermediate load efficiencies of buck converters with planar nonlinear inductors and variable on time control," *IEEE Trans. Power Electron.*, vol. 27, no. 1, pp. 342–353, Jan. 2012.

[8] L. Wang, Z. Hu, Y. Qiu, H. Wang, and Y. Liu, "A new model for designing multi-hole multi-permeability nonlinear LTCC inductors," in *Proc. IEEE Appl. Power Electron. Conf.*, Mar. 2014, pp. 757–762.

[9] E. Dallago, M. Passoni, and G. Venchi, "Analysis of high-frequency IGBT soft switching buck converter with saturable inductors," *IEEE Trans. Power Electron.*, vol. 22, no. 2, pp. 407–416, Mar. 2007.

[10] J. Sun, S. Hamada, J. Yoshitsugu, B. Guo, and M. Nakaoka, "Zero voltage soft-commutation PWM DC-DC converter with saturable reactor switch-cascaded diode rectifier," *IEEE Trans. Circuits Syst. I*, vol. 45, no. 4, pp. 348–354, Apr. 1998.

[11] S. Hamada and M. Nakaoka, "Family of saturable reactor assisted soft-switching PWM DC–DC convertors," *Proc. Inst. Electr. Eng.*, vol. 139, pp. 395–401, Jul. 1992.

[12] M. Stadler and J. Pforr, "Zero-voltage switched multi-phase converter utilizing nonlinear and coupled inductors," in *Proc. IEEE Appl. Power Electron. Conf.*, Feb. 2007, pp. 1038–1042.

[13] ST50-267, One of Composite Cores from Micrometals, Inc. (2015). [Online]. Available: http://www.micrometals.com/pcparts/ccore.html?zoom_highlight=ST50-267

[14] H. Ahmed, H. Cha, S. Kim, D. Kim, and H. Kim, "Wide load range efficiency improvement of a high power-density bidirectional DC-DC converter using an MR fluid-gap inductor," *IEEE Trans. Ind. Appl.*, vol. 51, no. 4, pp. 3216–3226, Jul. 2015.

[15] D. W. Kim, H. Cha, S. Lee, and D. H. Kim, "Characteristic of a variable inductor using magnetorheological fluid for efficient power conversion," *IEEE Trans. Magn.*, vol. 49, no. 5, pp. 1901–1904, May 2013.

[16] J. Sun, M. Xu, Y. Ren, and F. C. Lee, "Light-load efficiency improvement for buck voltage regulators," *IEEE Trans. Power Electron.*, vol. 24, no. 3, pp. 742–751, Mar. 2009.

[17] W. H. Wölfle and W. G. Hurley, "Quasi-active power factor correction with a variable inductive filter: theory, design and practice," *IEEE Trans. Power Electron.*, vol. 18, no. 1, pp. 248–255, Jan. 2003.

[18] Magnetics, "Step-gap E core swing chokes," *Tech. Bulletin, FC-S4*, 2001.

[19] ST, "Design tips for L6561 power factor corrector in wide range," *Appl. Note, AN1214*, Dec. 2000.

[20] C. R. Hanna, "Design of reactances and transformers which carry direct current," *J. Amer. Inst. Electr. Eng.*, vol. 46, pp. 155–160, Feb. 1927.

[21] T. Ge, K. Ngo, J. Moss, and M. Lim, "Gap design for nonlinear ferrite cores to maximize inductance," in *Proc. IEEE Energy Convers. Congr. Expo.*, Sep. 2014, pp. 5237–5242.

[22] N. Mohan, T. M. Undeland, and W. P. Robbins, *Power Electronics-Converters, Applications, and Design*, 2nd ed. Chichester, U.K.: Wiley, 1995.

[23] M. Lu and K. D. T. Ngo, "Model for electromagnetic actuator with significant fringing using minimal fitting parameters," *IEEE Trans. Magn.*, vol. 51, no. 1, pp. 1–7, Jul. 2014.

[24] V. C. Valchev, A. P. Van Den Bossche, and D. M. Van De Sype, "Ferrite losses of cores with square wave voltage and dc bias," in *Proc. IEEE Conf. Ind. Electron. Soc.*, Nov. 2005, pp. 837–841.

[25] C. A. Baguley, B. Carsten, and U. K. Madawala, "An investigation into the impact of DC bias conditions on ferrite core losses," *IEEE Trans. Magn.*, vol. 44, no. 2, pp. 246–252, Feb. 2008.

[26] C. A. Baguley, U. K. Madawala, and B. Carsten, "The impact of vibration due to agnetostriction on the core losses of ferrite toroidals under DC bias," *IEEE Trans. Magn.*, vol. 47, no. 8, pp. 2022–2028, Aug. 2011.

[27] J. Mühlethaler, J. Biela, J. W. Kolar, and A. Ecklebe, "Core losses under DC bias condition based on Steinmetz parameters," in *Proc. IEEE/IEEJ Int. Power Electron. Conf.*, Jun. 2010, pp. 2430–2437.

[28] K. Venkatachalam, C. R. Sullivan, T. Abdallah, and H. Tacca, "Accurate prediction of ferrite core loss with nonsinusoidal waveforms using only Steinmetz parameters," in *Proc. IEEE Workshop Comput. Power Electron.*, 2002, pp. 36–41.

[29] J. Mühlethaler, J. Biela, J. W. Kolar, and A. Ecklebe, "Improved core loss calculation for magnetic components employed in power electronic systems," in *Proc. IEEE Appl. Power Electron. Conf.*, Mar. 2011, pp. 1729–1736.

[30] A. Brockmeyer, "Experimental evaluation of the influence of DC premagnetization on the properties of power electronic ferrites," in *Proc. IEEE Appl. Power Electron. Conf.*, Mar. 1996, pp. 454–460.

[31] C. A. Baguley, B. Carsten, and U. K. Madawala, "The effect of DC bias conditions on ferrite core losses," *IEEE Trans. Magn.*, vol. 44, no. 2, pp. 246–252, Feb. 2008.

[32] W. K. Mo, D. K. W. Cheng, and Y. S. Lee, "Simple approximations of the DC flux influence on the core loss power electronic ferrites and their use in design of magnetic components," *IEEE Trans. Magn.*, vol. 44, no. 6, pp. 788–799, Dec. 1997.

[33] C. Simão, N. Sadowski, N. J. Batistela, and J. P. A. Bastos, "Evaluation of hysteresis losses in iron sheets under DC-biased inductions," *IEEE Trans. Magn.*, vol. 45, no. 3, pp. 1158–1161, Mar. 2009.

[34] M. Mu, Q. Li, D. Gilham, F. C. Lee, and K. D. T. Ngo, "New core loss measurement method for high frequency magnetic materials," in *Proc. IEEE Energy Convers. Congr. Expo.*, Sep. 2010, pp. 4384–4389.

[35] M. Mu, F. Zheng, Q. Li, and F. C. Lee, "Finite element analysis of inductor core loss under DC bias conditions," *IEEE Trans. Power Electron.*, vol. 28, no. 9, pp. 4414–4421, Sep. 2013.

[36] J. Reinert, A. Brockmeyer, and R. De Doncker, "Calculation of losses in ferro- and ferrimagnetic materials based on the modified Steinmetz equation," *IEEE Trans. Inst. Appl.*, vol. 37, no. 4, pp. 1055–1061, Jul./Aug. 2001.

[37] J. Li, T. Abdallah, and C. R. Sullivan, "Improved calculation of core loss with nonsinusoidal waveforms," in *Proc. Ind. Appl. Conf.*, Sep./Oct. 2001, vol. 4, pp. 2203–2210.

[38] K. Venkatachalam, C. R. Sullivan, T. Abdallah, and H. Tacca, "Accurate prediction of ferrite core loss with nonsinusoidal waveforms using only Steinmetz parameters," in *Proc. IEEE Workshop Comput. Power Electron.*, Jun. 2002, pp. 36–41.

[39] M. Mu and F. C. Lee, "A new core loss model for rectangular AC voltages," in *Proc. IEEE Energy Convers. Congr. Expo.*, Sep. 2014, pp. 5214–5220.

[40] D. Lin, P. Zhou, W. N. Fu, Z. Badics, and Z. J. Cendes, "A dynamic-core loss model for soft ferromagnetic and power ferrite materials in transient finite element analysis," *IEEE Trans. Magn.*, vol. 40, no. 2, pp. 1318–1321, Mar. 2004.

[41] J. Hu and C. R. Sullivan, "AC resistance of planar power inductors and the quasidistributed gap technique," *IEEE Trans. Power Electron.*, vol. 16, no. 4, pp. 558–567, Jul. 2001.

[42] M. Mu, Q. Li, D. J. Gilham, F. C. Lee, and K. D. T. Ngo, "New core loss measurement method for high-frequency magnetic materials," *IEEE Trans. Power Electron.*, vol. 29, no. 8, pp. 4374–4381, Aug. 2014.

Ting Ge (S'13) received the B.S. degree in electrical engineering from the Huazhong University of Science and Technology, Wuhan, Hubei, China, in 2012. He is currently working toward the Ph.D. degree at the Center for Power Electronics Systems, Virginia Tech, Blacksburg, VA, USA.

His research interests include high-density magnetic components and high-frequency converter design.

Khai D. T. Ngo (S'82–M'84–SM'02–F'15) received the B.S. degree in electrical and electronics engineering from California State Polytechnic University, Pomona, CA, USA, in 1979, and the M.S. and Ph.D. degrees in electrical and electronics engineering from the California Institute of Technology, Pasadena, CA, in 1980 and 1984, respectively.

He was a Member of the Technical Staff at General Electric Corporate Research and Development Center, Schenectady, NY, USA, from 1984 to 1988. Between 1988 and 2006, he was with the University of Florida, Gainesville, USA. He is currently a Professor of electrical and computer engineering at Virginia Tech, Blacksburg, VA, USA, where he pursues technologies for integration and packaging of power passive and active components to realize building blocks for power electronic systems. These technologies lead to power conversion systems with higher efficiency and higher power density. His research interests include topologies, control, emission, and integration issues for RF power converters. Other research interests include magnetic materials and components, energy reclamation, and power integrated circuits.

Jim Moss (M'12) received the B.S.E.E. degree from Illinois Institute of Technology, Chicago, IL, USA, in 1977, and the M.S.E.M. degree from Santa Clara University, Santa Clara, CA, USA, in 1984.

He is currently the Power Products Technology Manager with Texas Instruments Silicon Valley Analog, Santa Clara, CA, USA. He is currently working on high-power modules utilizing controllers, MOS and GaN FETs, and passives. He has more than 35 years of experience in the semiconductor industry and with TI/National for more than 25 years. His experience covers power, wireless/RF, x86, and microcontrollers. He worked in systems design, product, test and various technical management roles. He holds an MSEM from Santa Clara University and BSEE from the Illinois Institute of Technology.